PAPER

Morphology-conserved transformation: synthesis of hierarchical mesoporous nanostructures of Mn_2O_3 and the nanostructural effects on Li-ion insertion/deinsertion properties†

Yongcai Qiu,[ab] Gui-Liang Xu,[c] Keyou Yan,[ab] Hui Sun,[b] Junwu Xiao,[b] Shihe Yang,*[ab] Shi-Gang Sun,[c] Limin Jin[d] and Hong Deng[d]

By means of morphology-conserved transformation, we have synthesized hierarchically structured Mn_2O_3 nanomaterials with different morphologies and pore structures. The key step of this method consists of the formation of a precursor containing the target materials interlaced with the judiciously chosen polyol-based organic molecules, which are subsequently knocked out to generate the final nanomaterials. In the present work, two kinds of precursor morphologies, oval-shaped and straw-sheaf-shaped, have been selectively prepared by hydrothermal treatment of different functional polyol molecules (oval-shape with fructose and straw-sheaf-shape with β-cyclodextrin) and potassium permanganate. Thermal decomposition of the precursors resulted in the formation of mesoporous Mn_2O_3 maintaining the original morphologies, as revealed by extensive characterization. These novel hierarchical nanostructures with different pore sizes/structures prompted us to examine their potential as anode materials for lithium ion batteries (LIBs). The electrochemical results with reference to LIBs show that both of our mesoporous Mn_2O_3 nanomaterials deliver high reversible capacities and excellent cycling stabilities at a current density of 200 mA g^{-1} compared to the commercial Mn_2O_3 nanoparticles. Moreover, the straw-sheaf-shaped Mn_2O_3 exhibits a higher specific capacity and a better cycling performance than the oval-shaped one, due to the relatively higher surface area and the peculiar nanostrip structure resulting in the reduced length for lithium ion diffusion. Morphology-conserved transformation yields two kinds of hierarchical mesoporous Mn_2O_3 nanomaterials with high capacities and cycling stabilities for lithium ion batteries.

1. Introduction

Over the past few years, the interest in the fabrication of transition metal oxide nanomaterials has soared owing to their potential value in gas sensors, optical and magnetic materials, energy management, and catalysis.[1–13] The development of transition metal oxide materials with new morphologies at meso- to nano-scales and the resulting enhanced properties is noted to be one of the substantive challenges in materials science and technology. Particularly, manganese oxides are not only promising electrode materials for Li-ion batteries and super-capacitors,[14–20] but also potent catalysts for oxidation of methane and selective-reduction of nitrobenzene and others important in air purification processes.[21–23] As of now, much effort has been invested to produce manganese oxide nanostructures with distinct morphologies as well as mesoporous structures characterized by large specific surface areas. Generally, these methods for preparing mesoporous nanomaterials involve the formation of an original template using mesoporous silicas as hard templates or organized polymers as soft templates, followed by the deposition of materials of interest within the pores and the subsequent removal of the templates.[24–28] Although the template-assisted methods are able to synthesize different mesoporous materials, the complicated synthetic procedures are commonly high-cost, low-yield, and time-consuming, thus hindering their large-scale industrial applications. In addition, the resulting morphologies from the template methods are not well-controlled at the nanoscale. This situation entails efforts to develop alternate methods, potentially more effective and economical, for preparing porous nanomaterials.

[a]Nano Science and Technology Program, The Hong Kong University of Science and Technology, Clear Water Bay, Kowloon, Hong Kong, P.R. China. E-mail: chsyang@ust.hk
[b]Department of Chemistry, The Hong Kong University of Science and Technology, Clear Water Bay, Kowloon, Hong Kong, P.R. China
[c]State Key Laboratory of Physical Chemistry of Solid Surfaces, Department of Chemistry, College of Chemistry and Chemical Engineering, Xiamen University, Xiamen, 361005, China
[d]School of Chemistry & Environment and Key Laboratory of Electrochemical Technology on Energy Storage and Power Generation of Guangdong Higher Education Institutes, South China Normal University, Guangzhou, 510006, China
† Electronic supplementary information (ESI) available. See DOI: 10.1039/c1jm00011j

6346 | *J. Mater. Chem.*, 2011, **21**, 6346–6353

This journal is © The Royal Society of Chemistry 2011

It has been realized in the last few years that metal-based intermediate compounds, such as metal carbonates, hydroxides, oxyhydroxides and hydroxide-carbonates,[29–36] as well as metal coordination polymers[37–39] can be transformed *via* thermal decomposition into mesoporous metal oxide nanostructures with conserved morphologies. This forms the basis of morphology-conserved transformation for the generation of unusual meso-porous nanostructures, which can be complementary to porous structures fabricated by the template-assisted methods. Chief among the advantages of the morphology-conserved trans-formation method is its simplicity. With this method, the prep-aration of mesoporous transition metal oxides only involves two steps: the precursor formation, *e.g.*, by a one-step hydrothermal approach, and the generation of the mesoporous nanostructures by, for example, calcination. Moreover, precursors can be prepared with tailored morphologies to be transcribed to the final products by the reactions of metal salts with appropriate complex anionic groups with versatile molecular functionalities including pore-forming characteristics. Some interesting work has already been appeared in advancing the morphology-conserved transformation method. For example, Suib and co-workers reported the synthesis of semiconducting mixed-valent manganese oxide mesoporous structure, which is gener-ated from calcination of a precursor including $Mn(OH)_2$.[30] Lou *et al.* prepared electrochemically active Co_3O_4 with a needle-like nanotube morphology through a novel self-supported topotactic transformation from a β-$Co(OH)_2$ precursor in nanoneedle shape.[31] A porous hollow MO_x structure was prepared from acid dissolution of a core@shell structure, *e.g.*, $MCO_3@MO_x$ (M = Mn, Ni, Fe, *etc.*), by controlled thermal decomposition of the precursor, *e.g.*, MCO_3.[31] Oh *et al.* reported the synthesis of micrometre-sized ZnO hexagonal rings by thermal treatment of hexagonal disks of zinc coordination-polymer.[39] More recently, we reported mesoporous single-crystalline ZnO nano-plates obtained from thermal decomposition of a nanoscale plate-like precursor [hydrozincite $Zn_5(CO_3)_2(OH)_6$].[33]

Because of its simplicity and cost-effectiveness, the morphology-conserved transformation has become one of the most important methods for preparing porous transition metal oxides with intriguing nanostructures and unusual electronic, magnetic, gas sensing, catalytic and other properties,[29–39] as well as a general approach for fabricating porous film based nano-devices, such as chemical and biological sensors and dye-sensi-tized solar cells.[33,40–43] Our group has been interested in developing mesoporous nanostructures by using the morphology-conserved transformation approach for electro-chemical and photoelectrochemical applications.[33,38,44] One of the objectives of the current work was to broaden the scope of the morphology-conserved transformation approach by extending it to the synthesis of hierarchical mesoporous structures.

Hierarchical mesoporous structures are ideal for electrodes of lithium ion batteries (LIBs) because they could both reduce agglomeration during electrochemical cycling and decrease interfacial contact resistance. These features are not shared by nanoparticles, which are apt to form agglomerates and very difficult to disperse and mix with carbon additives and binders, resulting in performance failing accompanied by a large increase in contact resistance between the film and the electrode. In addition, the hierarchical structure containing numerous large voids should facilitate electrolyte access and Li-ion diffusion. Therefore, the development of a facile method for preparing hierarchical mesoporous structures is a significant issue for their practicable implementation in LIBs.

In this paper, we look closely into the preparation of porous manganese oxides by morphology-conserved transformation and their application with regard to Li-ion storage. Regarding the synthesis, we chose fructose ($C_6H_{12}O_6$) and β-CD (CD = cyclodextrin ($C_6H_{10}O_5$)$_7$) as multifunctional reagents for both structural control and pore formation. Fructose is a mono-saccharide while β-CD is a cyclic saccharide, and both contain numerous OH^- groups and thus can act as bridging ligands for assembling nanoscale building units so as to control the morphology. Moreover, the ligands can be oxidized by MnO_4^-, added as a co-reagent, to produce CO_2 and/or carboxylate groups at appropriate temperatures, potentially generating unusual nanostructures. Two kinds of morphologies, oval-sha-ped and straw-sheaf-shaped, were generated by hydrothermal treatment of a $KMnO_4$ and fructose mixture and a $KMnO_4$ and β-CD (CD = cyclodextrin) mixture, respectively. The final products were readily obtained by morphology-conserved thermal treatment in air. With these novel nanomaterials, we have also first studied the effects of nanostructures on their electrochemical performances when used as anode materials for lithium ion batteries (LIBs).

2. Experimental procedures

In a typical synthesis, 1 g of $KMnO_4$ and 60 mL of 20 g L^{-1} fructose (or β-cyclodextrin) were mixed under magnetic stirring. After 30 min stirring, the mixture was transferred and sealed in a 100 mL Teflon-lined autoclave, heated at 180 °C for 10 h, and finally cooled to room temperature. The precipitate was collected by filtration, washed alternately with deionized water and ethanol three times, and dried in air at ambient condition. Finally, the products were subjected to heat treatment in air at 600 °C for 2 h.

The as-prepared products were characterized by scanning electron microscopy (SEM), transmission electron microscopy (TEM) and powder X-ray diffraction (XRD) measurements. The morphologies were directly examined by SEM using a JEOL 6700F at an accelerating voltage of 5 kV. For TEM observations, the products were ultrasonically dispersed in ethanol and then dropped onto carbon-coated copper grids. TEM observations were carried out on JEOL 2010F and JEOL 2010 microscopes both operating at 200 kV. An energy-dispersive X-ray spec-trometer (EDX) was attached to the JEOL 2010F. The XRD analyses were performed on a Philips PW-1830 X-ray diffrac-tometer with Cu Kα radiation (λ = 1.5406 Å) at a scanning speed of 0.025° s^{-1} over the 2θ range of 10–70°. The BET surface area was characterized using a Coulter SA 3100 surface area analyzer.

The electrodes were fabricated by using the Mn_2O_3 meso-materials as the active materials, conductive carbon blacks (Super-P) and polyvinylidene fluoride (PVDF) binder in a weight ratio of 80 : 10 : 10. The slurry was coated on a copper foil and dried overnight in a vacuum at 100 °C. Electrochemical studies were characterized in CR2016-type coin cell. Test cells were assembled in an argon-filled glove box with water and oxygen contents less than 1 ppm. Li foil was used as the counter electrode

and polypropylene (PP) film (Celgard 2400) as the separator. The electrolyte was 1 M $LiPF_6$ in a mixture of EC/DEC/DMC in a volume ratio of 1 : 1 : 1 with 2 wt% vinylene carbonate (VC) as additive.

3. Results and discussion

The powder X-ray diffraction (XRD) pattern in Fig. 1a shows the precursor of I can be indexed to the rhombohedral structure of $MnCO_3$ ($R\bar{3}c$) with lattice constants $a = 4.690$ Å, $c = 15.552$ Å, in good agreement with the reported values (JCPDS Card 00-002-0785). Fig. 2a shows the general scanning electron microscopy (SEM) morphology of the as-prepared precursor obtained after hydrothermal treatment of potassium permanganate and fructose. The precursor takes an oval-shaped microstructure with controlled grain sizes ranging from submicrometre to 3 μm. Judging from the transmission electron microscopy (TEM) images in Fig. 2b and the inset of Fig. 2a, these microparticles seem to be derived from oriented aggregation of numerous nanoparticles. Indeed, the selected-area electron diffraction (SAED) pattern (the inset of Fig. 2b) exhibits a set of regular spots. In addition, the high-resolution TEM (HRTEM) image in Fig. 2c clearly shows the lattice fringes spanning the entire length of the microcrystal with a d-spacing of 2.0 Å, which corresponds to the (202) plane of the rhodochrosite. This is also supported by the Fast Fourier Transforms of the images (the inset of Fig. 2c).

Fig. 3a shows a straw-sheaf-shaped microstructure. The precursor of II was obtained after hydrothermal treatment of potassium permanganate and β-cyclodextrin. The main XRD peaks of the precursor in Fig. 1c can also be indexed to the rhombohedral structure of $MnCO_3$, while the minor peaks correspond to the manganite (MnOOH, JCPDS Card 01-074-1842). The microparticles are composed of a bundle of outspread nanostrips with lengths in the range of 500 nm to 3 μm, which are closely linked together in the middle (see Fig. 3b). A HRTEM image taken from the nanowire in Fig. 3b shows the clear and coherent lattice fringes with a d-spacing of 3.6 Å, corresponding to the (012) plane of the rhombohedral phase of $MnCO_3$.

The hydrothermal-derived precursors were further examined by FT-IR studies (Fig. S1† in the ESI). The broad bands centered

at around 3450 cm^{-1} and 1647 cm^{-1} are, respectively, ascribed to the O–H stretching and bending modes of the OH^- groups and/or water molecules. The bands around 1430, 850 and 723 cm^{-1} are the characteristic vibration band of CO_3^{2-}.[45] Next, both of the precursors were subjected to thermogravimetric (TG) analysis in air (Fig. 4). The first weight loss of 6.1% for I (2.6% for II) from room temperature to ~255 °C can be attributed to the removal of water molecules, while the second significant weight loss of 39.8% for I (33.2% for II) in the temperature range of 255–400 °C is most likely due to thermal decomposition of $MnCO_3$ or MnOOH into Mn_2O_3 and combustion of adsorbed organic species.

After thermal treatment at 600 °C for 2 h, the as-prepared precursors were completely transformed into α-Mn_2O_3 (JCPDS card no. 00-002-0896) on the basis of the XRD patterns in Fig. 1b and d. The sharp and strong XRD peaks also demonstrate the good crystallinity and high purity of the products. It should be noted that the microstructures in both samples were quite thermally stable without structural collapse (Fig. 2d and 3d). Fig. 2d shows SEM and TEM images of the oval-shaped Mn_2O_3. Indeed, the transformed mesoporous Mn_2O_3 microcrystals are rather intact composing of fine Mn_2O_3 nanoparticles with diameters ranging from 15 to 25 nm. Interestingly, the nanoparticles are closely packed and oriented in the same way, as confirmed by a set of electron diffraction spots in the SAED pattern (Fig. 2e and the inset of Fig. 2e). In addition, the lattice fringes with a d-spacing of 3.8 Å (see the HRTEM image in Fig. 2f) from different nanoparticles are parallel to each other, which are revealed in the Fast Fourier Transforms of the images (the inset of Fig. 2f). In a similar way, the straw-sheaf precursor was also converted into mesostructure after heat treatment. The SEM image in Fig. 3d shows the converted structure consisting of numerous porous nanostrips. The inset of Fig. 3d shows an enlarged image of a representative straw-sheaf microparticle. Notice that the surface of the microparticle in Fig. 3e became rough and slightly loose, but the microparticle is still held together as a whole. As can be seen from the higher magnification TEM image (Fig. 3f) taken from its edge (Fig. 3e), numerous pores indeed pass through the nanostrips. The lattice spacings of 2.3 Å and 3.8 Å are recognized and correspond to the inter-plane distances of (400) and (211) of the cubic phase of Mn_2O_3, respectively.

During the formation of metal-containing precursors, different polyol-based organic additives may influence the precursor morphologies by virtue of different coordination modes. Fig. 5 clearly illustrates the morphology changes with the increase of reaction times from 0.5, 3 and 5 h, respectively. Further discussion on the changes will be given below. According to the present results here and from other reports,[46–48] the following steps can be considered in understanding the formation mechanism of the mesoporous microparticles (Fig. 6). (i) Initially, the permanganate ions should be coordinated by the functional groups of the polyol-based organic molecules. (ii) Redox reactions between permanganates and polyol-based organic molecules (such as fructose and β-CD) would generate $MnCO_3$ and MnOOH precipitates (eqn (1)–(5)), which would nucleate under the capping of the polyol-based organic molecules. The chain-like fructose would assist the formation of the chain-like structure (Fig. 5a), whereas the cask-like β-CD would
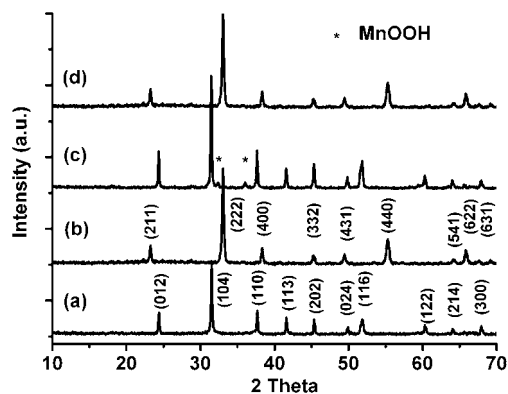

Fig. 1 X-Ray diffraction (XRD) patterns of the samples (a) before and (b) after heat treatment of the precursor of I, and (c) before and (d) after heat treatment of the precursor of II. The peaks marked by asterisks are attributed to MnOOH.
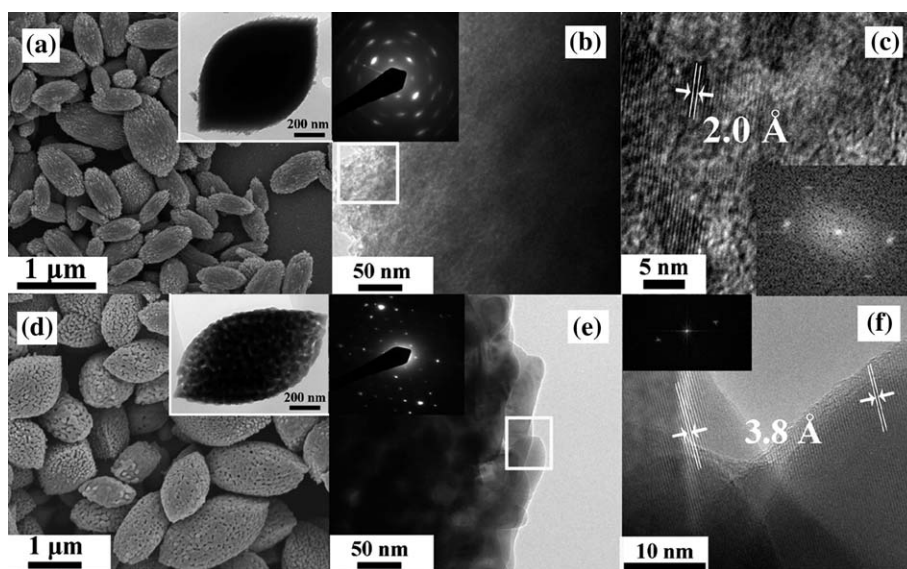
Fig. 2 (a) SEM and TEM (inset) images of the as-prepared precursor of I. (b) An enlarged TEM image taken from its edge and its corresponding SAED pattern (inset) of an oval-shaped $MnCO_3$. (c) A HRTEM image taken from (b) (marked with a square symbol) and its corresponding FFT pattern (inset). (d) SEM and TEM (inset) images after heat treatment of the precursor of I. (e) An enlarged TEM image taken from its edge and its corresponding SAED pattern of an oval-shaped Mn_2O_3. (f) A HRTEM image taken from (e) (marked with a square symbol) and its corresponding FFT pattern (inset).

tend to form the spherical nanoparticles (Fig. 5e). One can imagine that with the elapsing of reaction time, the chain-like structure would self-assemble into an oval-shaped microparticle (Fig. 5b), whereas the spherical nanoparticles would spontaneously aggregate into dumbbell-like microparticles (Fig. 5f). (iii) With further redox reactions, the resulting structures above would orient the constituent nanoparticles within the microparticles and grow into the respective precursors: the chain-like structure assembled microparticles would finally evolve into the

nanoparticle-based oval-shaped microstructure (Fig. 5c), whereas the particles assembled microparticles would finally form the nanostrip-based microstructure (Fig. 5g). Finally, on heating the precursors, numerous pores would be generated thanks to the release of CO_2 and the combustion of adsorbed organic species, as can be seen in (eqn (6) and (7)).

$$4R\text{--}CH_2OH + MnO_4^- \rightarrow MnOOH + 4R\text{--}CHO + OH^- + H_2O \qquad (1)$$
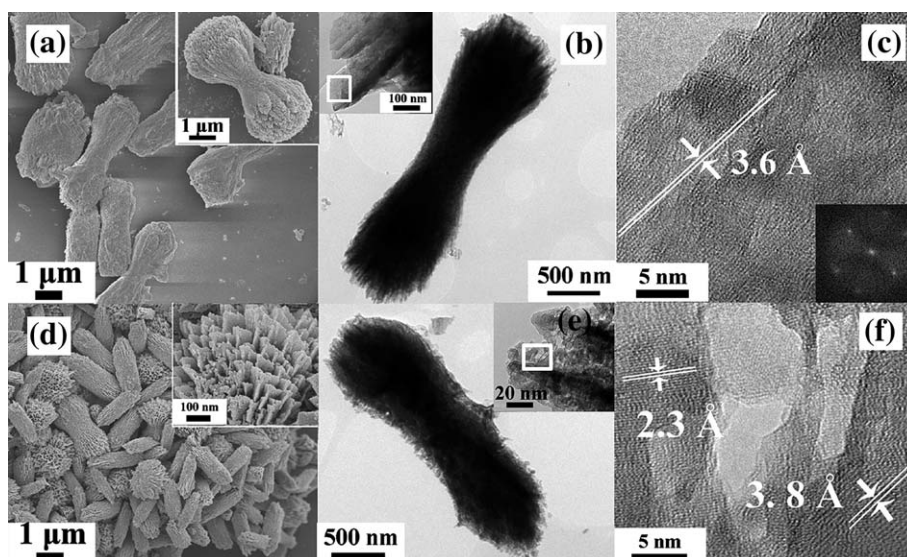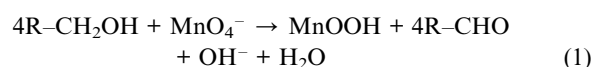

Fig. 3 (a) SEM image of the as-prepared precursor of II. The inset is an enlarged SEM of a representative straw-sheaf-shaped structure. (b) A TEM image of a representative straw-sheaf-shaped structure. The inset shows its edge structure. (c) A HRTEM image taken from the straw-sheaf in (b) (marked with a square symbol) and its corresponding FFT pattern (inset). (d) A SEM image after heat treatment of the precursor of II. The inset is the surface structure of a straw-sheaf-shaped microparticle. (e) A TEM image of (the inset shows the zoom-in image of the edge) a straw-sheaf obtained after heat treatment of the precursor of II. (f) A HRTEM image taken from the straw-sheaf in (e) (marked with a square symbol).
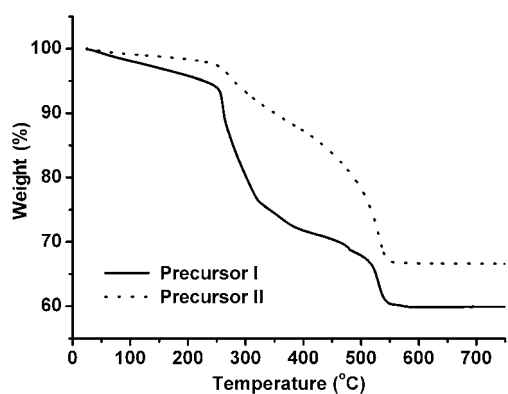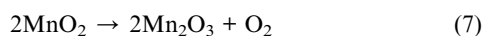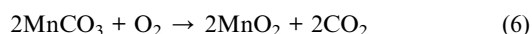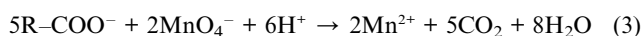
Fig. 4 TGA curves of as-prepared precursors of I and II.

$$R–CHO + MnO_4^- \rightarrow MnOOH + R–COO^- + H_2O \quad (2)$$

$$5R–COO^- + 2MnO_4^- + 6H^+ \rightarrow 2Mn^{2+} + 5CO_2 + 8H_2O \quad (3)$$

$$CO_2 + H_2O \rightarrow 2H^+ + CO_3^{2-} \quad (4)$$

$$Mn^{2+} + CO_3^{2-} \rightarrow MnCO_3 \quad (5)$$

$$2MnCO_3 + O_2 \rightarrow 2MnO_2 + 2CO_2 \quad (6)$$

$$2MnO_2 \rightarrow 2Mn_2O_3 + O_2 \quad (7)$$

Brunauer–Emmett–Teller (BET) gas-sorption measurements were performed at 77 K to investigate the textural properties of the Mn_2O_3 samples. Fig. 7 shows their N_2 adsorption/desorption isotherms. Both samples exhibit type IV N_2 isotherms with type-H_3 desorption hysteresis loops observed at the relative pressure of 0.6–0.9, suggesting the presence of mesopores formed due to the aggregation of particles.[49] The BET specific surface areas of both samples were measured to be 36.1 $m^2 g^{-1}$ and 52.3 $m^2 g^{-1}$ for
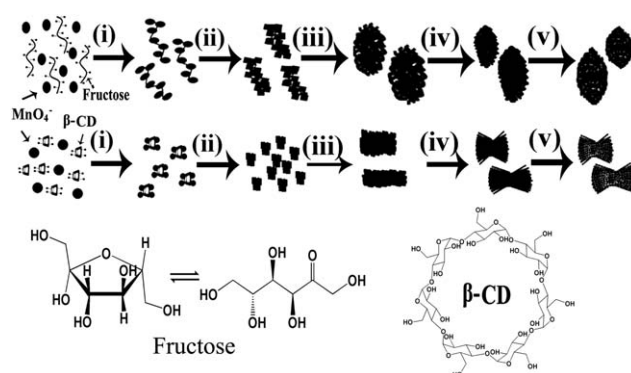

Fig. 6 Schematic diagram illustrating the growth mechanism of the mesoporous Mn_2O_3 microparticles. (i) First, the MnO_4^- ions assemble together with the functional fructose (or β-CD) molecules under the stirring condition; (ii) redox reactions between them yield chain-like (or particle-like) precipitates; (iii) self-aggregation of the precipitates leads to the formation of oval-shaped structures (or dumbbell-like microparticles); (iv) further growth and maturation give rise to the resulting precursors; and (v) calcinations of the precursors produce the porous structures. Molecular structures of the fructose and the β-CD are also shown at the bottom.

samples I and II, respectively. From the pore distribution curves in the inset of Fig. 7a, the oval-shaped Mn_2O_3 microstructures have pore distributions in the region of 3–20 nm on the basis of the Barrett–Joyner–Halenda (BJH) method, whereas the straw-sheaf-shaped Mn_2O_3 microstructures in the inset of Fig. 7b show pore distributions in the range from 3 to 60 nm.

Knowing that nanoporous metal oxide materials have shown high structural stability for reversible Li-ion insertion reactions,[50,51] we tested the two types of porous Mn_2O_3 microstructures as active anode materials for LIBs. To our knowledge, there have been hitherto only few reports on Mn_2O_3 nanomaterial based anodes for LIBs.[52–54] Fig. 8a shows the discharge/charge
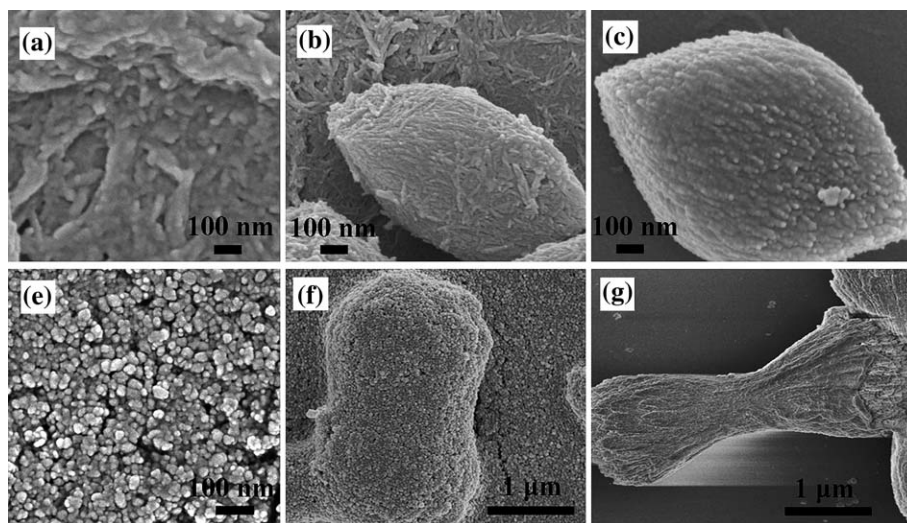

Fig. 5 SEM images of the precursors I and II grown at different reaction times of (a) 0.5, (b) 3 and (c) 5 h at 180 °C. (a)–(c) were obtained by using fructose and (e)–(g) were obtained by using β-CD.
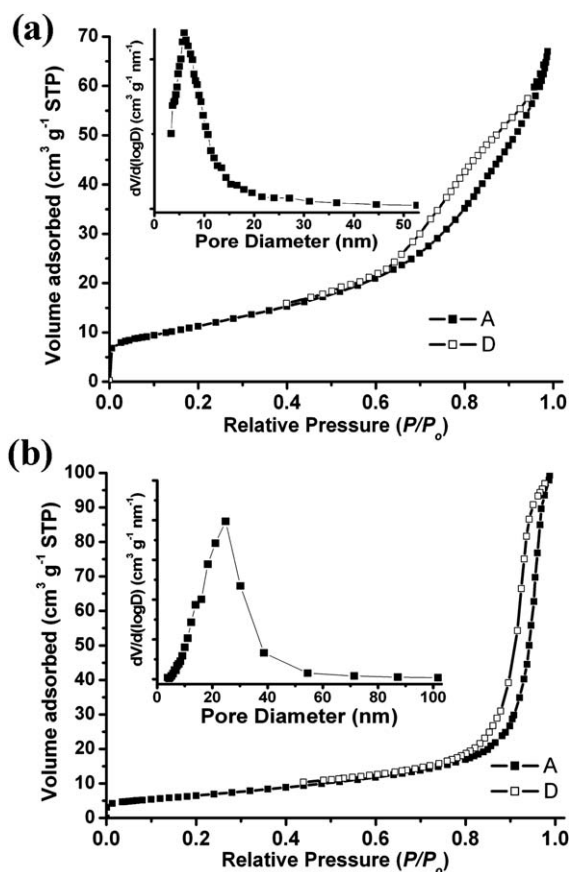
Fig. 7 N₂ sorption isotherms of the samples I (a) and II (b). Insets are their pore size distributions.

Fig. 8 (a) The first two discharge–charge curves of oval-shaped (solid lines), straw-sheaf-shaped (dashed lines) and commercial nanoparticulate (dotted lines) Mn_2O_3 between 0.01 and 2.5 V (vs. Li^+/Li) cycled at a constant current density of 200 mA g⁻¹. (b) Cycling performances for the electrodes of oval-shaped Mn_2O_3 (squares), straw-sheaf-shaped (circles) and commercial nanoparticulate (triangles) Mn_2O_3 between 0.01 and 2.5 V (vs. Li^+/Li) cycled at a constant current density of 200 mA g⁻¹.

curves of the two as-prepared Mn_2O_3 microstructures and commercial Mn_2O_3 nanoparticles in the first to 2nd cycles measured at a current density of 200 mA g⁻¹ at room temperature in a potential window between 0.01 and 2.5 V (vs. Li^+/Li). In the first discharge curves of the three different electrodes, the first voltage drops from 2.5 V to a plateau at about 0.3 V can be ascribed to the electrochemical lithium insertion reactions expressed by eqn (8) and (9). And then the voltage decreases slowly to 0.01 V, in correspondence to the complete reduction of Mn^{2+} to Mn^0 (see eqn (10)). For the initial charge curve, there appears a slope in the voltage range between 1.0 and 1.5 V, associated with the oxidation of Mn^0 back to Mn^{2+}. Discharge capacities of 1243, 1179 and 1159 mA h g⁻¹ for the first discharge cycle are obtained, respectively, from the nanoparticulate, straw-sheaf-shaped and oval-shaped Mn_2O_3 electrodes. Since the theoretical capacity of Mn_2O_3 is ∼1018 mA h g⁻¹, the excess capacities could be associated with the decomposition of the electrolyte at low voltages generating a solid electrolyte interphase (SEI) layer and the further lithium storage via interfacial charging at the metal/Li_2O interface.[52,53,55] As shown in Fig. 8a, in the subsequent discharge curves for the three Mn_2O_3 electrodes, the discharging plateaus up-shifted to 0.55 V should be ascribed to the reversible Li-ion insertion reaction in eqn (10), which has a theoretical reversible capacity of ∼755 mA h g⁻¹ and is actually the maximum reversible capacity attainable in any measurements.
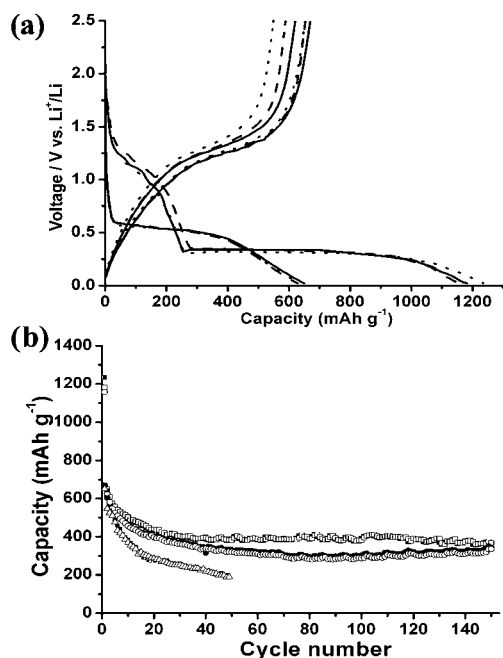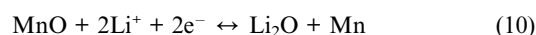
$$2Li^+ + 3Mn_2O_3 + 2e^- \rightarrow 2Mn_3O_4 + Li_2O \quad (8)$$

$$2Li^+ + Mn_3O_4 + 2e^- \rightarrow 3MnO + Li_2O \quad (9)$$

$$MnO + 2Li^+ + 2e^- \leftrightarrow Li_2O + Mn \quad (10)$$

The LIB cycling performances of the Mn_2O_3 products are shown in Fig. 8b. A fast capacity fading in the first 20 cycles was observed, possibly a result of the complicated side-reactions and/or irreversible structure transformation. Afterward, the capacity was generally retained because the electrochemically reversible structures for Li-ion insertion reaction have been established. The straw-sheaf-shaped Mn_2O_3 from 21 to 150 cycles delivered an average capacity of 400 mA h g⁻¹, even in the 150th cycle the capacity was still maintained at above 380 mA h g⁻¹, a value which is higher than the theoretical capacity of commercial graphite (372 mA h g⁻¹). Under the same testing conditions, a lower average capacity of 300 mA h g⁻¹ of the oval-shaped Mn_2O_3 from 21 to 150 cycles was obtained and after 150 cycles the capacity was ∼320 mA h g⁻¹. The worst of all was the commercial nanoparticulate Mn_2O_3 material (15 nm in diameter) which only delivered ∼200 mA h g⁻¹ after 50 cycles. Together, the straw-sheaf-shaped Mn_2O_3 displayed the best cycling performance not only among the Mn_2O_3 anode materials we tested but also those reported previously.[52–54] The large difference in the electrochemical results suggests that the good Li storage performance is a benefit from the specific morphology of Mn_2O_3. In other words, the straw-sheaf-shaped Mn_2O_3

This journal is © The Royal Society of Chemistry 2011

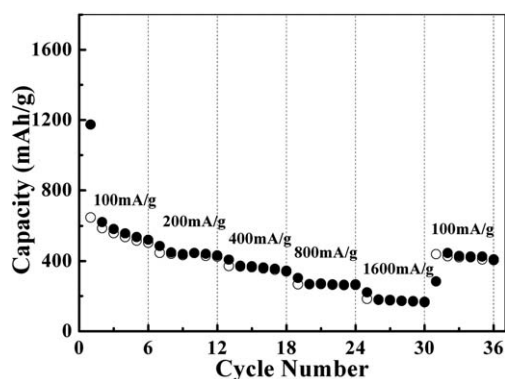*J. Mater. Chem.*, 2011, **21**, 6346–6353 | 6351

Fig. 9 Cycling specific capacity profile of straw-sheaf-shaped Mn_2O_3 at different charge/discharge rates.

comprised of numerous porous nanostrips features a much larger surface area and a much shorter Li-ion insertion length, which are held responsible for the high capacity and long cycling life-time for the corresponding LIBs. Conceivably, the hierarchical porous materials made of nano-size units can avoid agglomeration during electrochemical cycling and minimize interfacial contact resistance. Also, the nano-size units can provide more active sites and shorter diffusion lengths for lithium insertion/extraction than their large-size counterparts. The porosity of the materials, on the other hand, can facilitate electrolyte access and Li-ion diffusion. Moreover, the porous structure could also accommodate the large volume changes during lithium insertion/extraction, accounting for the significantly enhanced cycling performance of our Mn_2O_3 electrodes.

To better understand the electrochemical behavior of the straw-sheaf-shaped Mn_2O_3, we also investigated its rate performance with respect to Li^+ insertion/extraction. As shown in Fig. 9, the material could deliver a specific capacity of $\sim$550 mA h g^{-1} at a current density of 100 mA g^{-1}, $\sim$440 mA h g^{-1} at 200 mA g^{-1}, 370 mA h g^{-1} at 400 mA g^{-1}, $\sim$270 mA h g^{-1} at 800 mA g^{-1} and $\sim$180 mA h g^{-1} at 1600 mA g^{-1}, respectively. Upon altering the current density back to 100 mA g^{-1}, the capacity of $\sim$430 mA h g^{-1} was recovered. This demonstrates the Mn_2O_3 nanostructure has a great potential as an anode material in LIBs.

4. Conclusions

In conclusion, the polyol-assisted hydrothermal synthesis and sequential thermal decomposition is a facile route to prepare the mesoporous metal oxides. By selectively employing two different functional polyol molecules and potassium permanganate, we have prepared two different precursors with distinct morphologies under hydrothermal conditions. The thermal decomposition leads to conversion of the precursor to the mesoporous structure. The virtues of this approach include its simplicity, cost-effectiveness, and complementary to template-assisted methods for the fabrication of porous nanostructures. Additionally, the mesoporous metal oxides have shown their favorable properties in applications as functional materials in LIBs. For example, the electrochemical behaviors with regard to Li storage demonstrate that our hierarchical mesoporous structures

of Mn_2O_3 have much higher reversible capacities and better cycling retention than the nanoparticles counterpart. Therefore, the morphology-conserved transformation will be an effective synthetic strategy in the preparation of other mesoporous structures with interesting structural and functional properties.

Acknowledgements

References

1 M. Tiemann, *Chem.–Eur. J.*, 2007, **13**, 8376.
2 Y. Tokura, *Curr. Opin. Solid State Mater. Sci.*, 1998, **3**, 175.
3 P. Poizot, S. Laruelle, S. Grugeon, L. Dupont and J.-M. Tarascon, *Nature*, 2000, **407**, 496.
4 Y. Rao and D. M. Antonelli, *J. Mater. Chem.*, 2009, **19**, 1937.
5 W. X. Zhang and S. H. Yang, *Acc. Chem. Res.*, 2010, **42**, 1617.
6 C. Xu, R. Wang, Y. Zhang and Y. Ding, *Nanoscale*, 2010, **2**, 906.
7 M. Woodhouse and B. A. Parkinson, *Chem. Soc. Rev.*, 2009, **38**, 197.
8 Y. C. Qiu, W. Chen and S. H. Yang, *Angew. Chem., Int. Ed.*, 2010, **49**, 3675.
9 A. Gurlo, *Nanoscale*, 2011, **3**, 154–165.
10 Y. F. Qiu and S. H. Yang, *Adv. Funct. Mater.*, 2007, **17**, 1345.
11 Y. C. Qiu, K. Y. Yan and S. H. Yang, *ACS Nano*, 2010, **4**, 6515.
12 Y. C. Qiu, W. Chen, S. H. Yang, B. Zhang, X. Zhang, Y. Zhong and K. S. Wong, *Cryst. Growth Des.*, 2010, **10**, 177.
13 C. M. Liu, L. Guo, R. M. Wang, Y. Deng, X. B. Xu and S. H. Yang, *Chem. Commun.*, 2004, 2726.
14 H. Jiang, T. Zhao, C. Yan, J. Ma and C. Z. Li, *Nanoscale*, 2010, **2**, 2195.
15 A. L. M. Reddy, M. M. Shaijumon, S. R. Gowda and P. M. Ajayan, *Nano Lett.*, 2009, **9**, 1002.
16 V. Subramanian, H. W. Zhu and B. Q. Wei, *Chem. Phys. Lett.*, 2008, **453**, 242.
17 C. Lin, J. A. Ritter and B. N. Popov, *J. Electrochem. Soc.*, 1999, **146**, 3155.
18 F. Cheng, Z. Tao, J. Liang and J. Chen, *Chem. Mater.*, 2008, **20**, 667.
19 W. Bowden, T. Bofinger, F. Zhang, N. Iltchev, R. Sirotina, H. Chen, C. Grey and S. Hackney, *J. Power Sources*, 2007, **165**, 609.
20 M. Winter and R. J. Brodd, *Chem. Rev.*, 2004, **104**, 4245.
21 E. R. Stobbe, B. A. D. Boer and J. W. Geus, *Catal. Today*, 1999, **47**, 161.
22 E. Grootendorst, Y. Verbeek and V. Ponce, *J. Catal.*, 1995, **157**, 706.
23 M. Baldi, E. Finocchio, F. Milella and G. Busca, *Appl. Catal., B*, 1998, **16**, 43.
24 X. Q. Chen, Z. S. Li, J. H. Ye and Z. G. Zou, *Chem. Mater.*, 2010, **22**, 3583.
25 M. Titirici, M. Antonietti and A. Thomas, *Chem. Mater.*, 2006, **18**, 3808.
26 P. Yang, D. Zhao, D. I. Margolese, B. F. Chmelka and Galen D. Stucky, *Chem. Mater.*, 1999, **11**, 2813.
27 P. Yang, D. Zhao, D. I. Margolese, B. F. Chmelka and G. D. Stucky, *Nature*, 1998, **396**, 152.
28 Y. D. Xia, Z. X. Yang and R. Molaya, *Nanoscale*, 2010, **2**, 639.
29 J. Liu, H. Xia, L. Lu and D. F. Xue, *J. Mater. Chem.*, 2010, **20**, 1506.
30 Z.-R. Tian, W. Tong, J.-Y. Wang, N.-G. Duan, V. V. Krishnan and S. L. Suib, *Science*, 1997, **276**, 926.
31 X. W. Lou, D. Deng, J. Y. Lee, J. Feng and L. A. Archer, *Adv. Mater.*, 2008, **20**, 258.
32 X. W. Xie and W. J. Shen, *Nanoscale*, 2009, **1**, 50.
33 Y. C. Qiu, W. Chen and S. H. Yang, *J. Mater. Chem.*, 2010, **20**, 1001.
34 L. Wang, F. Tang, K. Ozawa, Z.-G. Chen, A. Mukherj, Y. Zhu, J. Zou, H.-M. Cheng and G. Q. Lu, *Angew. Chem., Int. Ed.*, 2009, **48**, 7048.
35 M. M. Mohamed, W. A. Bayoumya, M. Khairya and M. A. Mousa, *Microporous Mesoporous Mater.*, 2008, **109**, 445.

36 X. W. Lou, D. Deng, J. Y. Lee and L. A. Archer, *J. Mater. Chem.*, 2008, **18**, 4397.

37 C. Y. Su, A. M. Goforth, M. D. Smith, P. J. Pellechia and H.-C. zur Loye, *J. Am. Chem. Soc.*, 2004, **126**, 3576.

38 Y. C. Qiu, S. H. Yang, H. Deng, L. M. Jin and W. S. Li, *J. Mater. Chem.*, 2010, **21**, 4439.

39 S. Jung, W. Cho, H. J. Lee and M. Oh, *Angew. Chem., Int. Ed.*, 2009, **48**, 1459.

40 X. He and D. Antonelli, *Angew. Chem., Int. Ed.*, 2002, **41**, 214.

41 Z.-M. Qi, I. Honma and H. Zhou, *J. Phys. Chem. B*, 2006, **110**, 10590.

42 Q. F. Zhang, T. P. Chou, B. Russo, S. A. Jenekhe and G. Z. Cao, *Angew. Chem., Int. Ed.*, 2008, **47**, 2402.

43 G. W. Zhou, Y. J. Chen, J. H. Yang and S. H. Yang, *J. Mater. Chem.*, 2007, **17**, 2839.

44 Y. C. Qiu, K. Y. Yan and S. H. Yang, *Chem. Commun.*, 2010, **46**, 8359.

45 X. C. Duan, J. B. Lian, J. M. Ma, T. Kim and W. J. Zheng, *Cryst. Growth Des.*, 2010, **10**, 4449.

46 S. Ashokaa, G. Nagarajua and G. T. Chandrappa, *Mater. Lett.*, 2010, **64**, 2538.

47 N. Baccile, G. Laurent, F. Babonneau, F. Fayon, M. Titirici and M. Antonietti, *J. Phys. Chem. C*, 2009, **113**, 9644.

48 X. Wang and Y. D. Li, *Mater. Chem. Phys.*, 2003, **82**, 419.

49 S. J. Gregg and K. S. W. Sing, in *Adsorption, Surface Area and Porosity*, Academic Press, London, UK, 2nd edn, 1982.

50 I. Moriguchi, R. Hidaka, H. Yamada, T. Kudo, H. Murakami and N. Nakashima, *Adv. Mater.*, 2006, **18**, 69.

51 J. Zhao, Z. Tao, J. Liang and J. Chen, *Cryst. Growth Des.*, 2008, **8**, 2799.

52 Y. Cai, S. Liu, X. Yin, Q. Hao, M. Zhang and T. Wang, *Physica. E*, 2010, **43**, 70–75.

53 M. Au and T. Adams, *J. Mater. Res.*, 2010, **25**, 1649.

54 S. Nayak, S. Malik, S. Indris, J. Reedijk and A. K. Powell, *Chem.–Eur. J.*, 2010, **16**, 1158.

55 J. Jamnik and J. Maier, *Phys. Chem. Chem. Phys.*, 2003, **5**, 5215.

This journal is © The Royal Society of Chemistry 2011

J. Mater. Chem., 2011, **21**, 6346–6353 | 6353